



Supplement of

Chemical composition and radiative properties of nascent particulate matter emitted by an aircraft turbofan burning conventional and alternative fuels

Miriam Elser et al.

Correspondence to: Miriam Elser (miriam.elser@empa.ch)

The copyright of individual parts of the supplement might differ from the CC BY 4.0 License.

S1 Methods

S1.1 Experimental set-up

This section contains a detailed description of the experimental set-up shown in Fig. 1. The engine exhaust was sampled at the engine exit plane using a single point sampling probe. The sample flow was then split into three sampling lines: the PM line (for measurements of particulate matter, PM), the GenTox line (for the sampling of genotoxic compounds) and the Annex 16 line (for measurements of the gaseous emissions and smoke certification, as specified in the ICAO Annex 16, Volume-II (ICAO, 2017)). The PM line was diluted with dry synthetic air (dilution factor ~ 10) to prevent water condensation and coagulation of the particles in the sampling line that transfers the sample flow to the instrumentation room. The system deployed for the measurement of non-volatile PM (nvPM) was compliant with the new ICAO standard (ICAO, 2017) and included an AVL Particle Counter (APC, AVL, 489) for particle number measurements, a Micro Soot Sensor (MSS, AVL, Model 483) to determine black carbon (BC) mass concentrations, and a CO₂ analyzer (Thermo Fisher Scientific, Model 410I) to calculate the dilution factor and the emission indices. The PM line additionally hosted the measurements of the optical properties (as described in the main text), size distributions (with a Scanning Mobility Particle Sizer, SMPS, TSI, Model 3938), particle density (coupling a Differential Mobility Analyzer (DMA, TSI, Model 3080), a Centrifugal Particle Mass Analyzer (CPMA, Cambustion) and a Condensation Particle Counter (CPC, TSI, Model 3776)), as well as the filter sampler for analysis of elemental carbon (EC) and organic carbon (OC) (URG, Series 2000-30FVT), a transmission electron microscopy (TEM) grids sampler (homebuilt) for the study of particle composition and morphology, and a cell exposure chamber (NAVICIT) to study aircraft particulate related health effects (Jonsdottir et al., 2019). The standard gas-phase measurements in the Annex 16 line included total hydrocarbons (THC) by Flame Ionization Detection (Horiba, Model MEXA-1170FID), NO_x/SO₂/CO/CO₂/O₂ by Chemiluminescence Detection (CLD) and Non-dispersive Infrared Absorption (Horiba, PG-250), and NO/NO₂/NO_x by Chemiluminescence (Eco Physics, Model CLD-844 S hr). In addition, a homebuilt sampling system for Volatile Organic Carbon (VOC) was accommodated in the Annex 16 line to collect samples for Gas Chromatography-Mass Spectrometry (GC-MS) analysis.

S1.2 Filter samples for EC/OC analysis

The method for measuring EC and OC in PM samples collected on filters is based on the volatilization and oxidation of carbon containing PM components with thermal-optical correction for pyrolytic carbon (PC). Thermal-optical OC/EC analysis as performed using a Sunset Laboratory Inc. OC/EC instrument is a NIOSH recognized method for the determination of organic and elemental carbon on particulates collected on quartz fibre filters. To quantify the content of EC and OC in the samples collected on the quartz fibre filter, thermal volatilization and oxidation at defined temperatures are used. A modified NIOSH 5040 thermal optical transmittance protocol, summarized in Table S1 was used. The optical transmittance through the sample was used for the correction of pyrolysis of OC occurring during the temperature steps in inert carrier gas (Helium mode). In the He mode, the oven's temperature is increased stepwise up to a first maximum of 870 °C. OC either volatilizes from the filter, or chars on the filter and forms pyrolytic carbon. In the He/O₂ mode the quartz oven is first cooled to 550°C and a second temperature ramp with a final temperature of 930°C is used. In the He/O₂ mode, EC and PC oxidize off the filter. All gases evolved from the filter during He and He/O₂ mode are carried into a manganese dioxide oven where organic vapors are quantitatively converted to CO₂ gas. In the methanator oven CO₂ is quantitatively converted to methane and finally measured with a flame ionization detector (FID). The laser transmittance signal was used to correct pyrolysis of OC to PC, which can take place when OC is heated in the He mode. Not correcting for pyrolysis leads to an underestimation of OC and corresponding overestimation of EC. As the temperature ramp proceeds, the laser transmittance is monitored continuously. Any charring of the organic carbon results in a decrease of the

transmittance signal of the laser, whereas it increases when EC and/or PC oxidize. Hence, the correction determines the amount of carbon oxidizes in the He/O₂ mode that is necessary to return the transmittance signal back to the initial value before pyrolysis started. The split point is defined as the split point when the transmittance returns to the initial value. The primary assumption for this correction is that the particulate elemental carbon and the pyrolytically formed elemental carbon have the same absorption coefficient.

An important component of the measurement system is the incorporation of a fixed volume loop which is used to inject an internal standard (5 % Methane in Helium) at the end of every analysis. Having every sample correlated to an internal standard, small variations in instrument performance are normalized and a very stable, repeatable analytical method for EC and OC results. Because there are no traceable primary reference materials available for EC and OC, calibration is limited to total carbon (TC). The principal calibration of the analytical system is conducted via TC values provided by blank filter samples spiked with calibration solutions of pure organic compounds such as sucrose. Additionally external calibration gas injections with methane (testing the FID) and CO₂ (testing the methanator and the FID) were also used.

The detection limit of the thermal-optical OC/EC analyzer is 0.2 µg C cm⁻² of filter.

Carrier Gas	Duration (sec)	Temperature (°C)
He	80	310
He	80	475
He	80	615
He	110	870
He	45	550
He/O ₂	45	550
He/O ₂	45	625
He/O ₂	45	700
He/O ₂	45	775
He/O ₂	45	850
He/O ₂	60	870
He/O ₂	120	930
CalGas + He/O ₂	120	No heat

Table S1. Modified NIOSH 5040 thermal-optical protocol used in this work. Note: An internal calibration is carried out at the end of each run oxidizing a known volume of methane (CH₄).

The EC/OC concentrations were calculated using three different split points (Auto Split; Oxygen Pt; 540s). Figure S1 shows the correlations between the EC mass and the photoacoustic measurement of BC mass with the MSS for the three split points. In our case, the split point was selected manually at 540 s based on operator expertise.

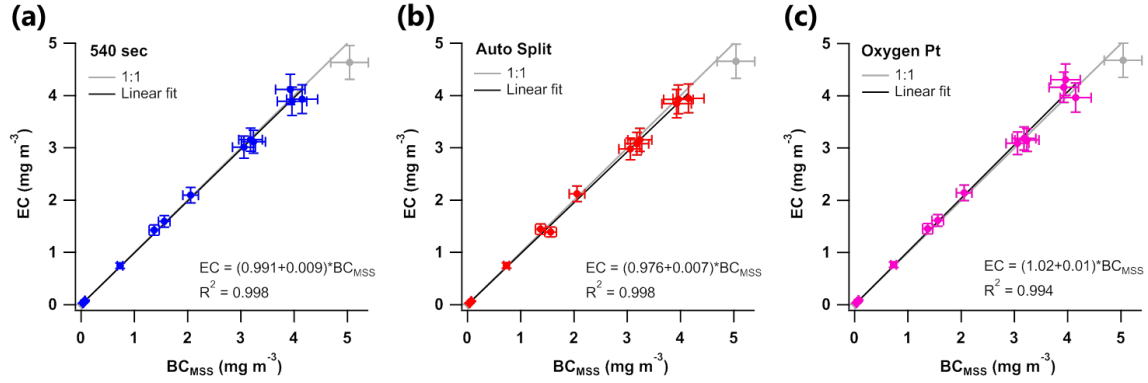


Figure S1. Scatter plot and linear regression lines of elemental carbon (EC) mass concentrations measured with the Sunset OC/EC Aerosol Analyzer and black carbon mass concentrations from the Micro Soot Sensor (BC_{MSS}) when using: (a) the manual split at 540 seconds, (b) the auto-split based on laser transmission, and (c) the Oxygen split point (which does not compensate for pyrolytic carbon, PC). Grey points indicate samples with a non-sharp limit of the sampling area that were therefore not used for the linear fit.

S1.3 Laboratory calibrations of the optical instruments

The Cavity Attenuated Phase Shift PM single scattering albedo monitor (CAPS PM_{ssa} , Aerodyne, $\lambda=532$ nm) and the Photo-Acoustic Extinctionmeter (PAX, Droplet Measurement Technologies, $\lambda=870$ nm) were calibrated in the laboratory prior to the measurements following standard operation procedures. The calibration particles (ammonium sulfate (AS) and nigrosin (Nig)) were generated with a TSI atomizer (model 306200) and diluted with HEPA filtered air to the desired mass concentrations (varied between $10 \mu g m^{-3}$ and up to $3 mg m^{-3}$). After passing a silica-gel column for drying, the particle stream was divided into three different lines to a Scanning Mobility Particle Sizer (SMPS, TSI model 3080) to measure the size distributions of the particles, and the two optical instruments. The results of the calibrations are summarized in Fig. S2. As for high engine thrust levels the CAPS scattering signal in the diluted PM line is out of the instrument linear range (i.e. above $1000 Mm^{-1}$), the scattering calibration was extended to the full measurement region (up to $6000 Mm^{-1}$) and the calibration curve was used to correct the scattering measurements.

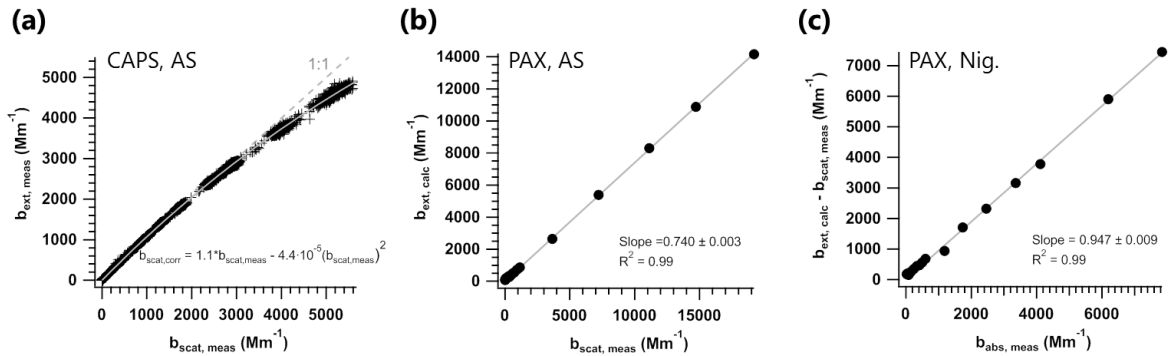


Figure S2. Laboratory calibrations of the Cavity Attenuated Phase Shift PM single scattering albedo monitor (CAPS) and the Photo-Acoustic Extinctionmeter (PAX): (a) Scatter plot and polynomial fit of the CAPS extinction and absorption coefficients (b_{ext} and b_{abs}) for measurements with ammonium sulfate (AS); (b) Scatter plot and linear fit of the PAX extinction and absorption coefficients (b_{ext} and b_{abs}) for measurements with ammonium sulfate (AS). (c) Scatter plot linear fit of the PAX extinction and absorption coefficients (b_{ext} and b_{abs}) for measurements with nigrosine ink (Nig).

In addition, a correction for the gas phase absorption is also required at the low measurement wavelength of the CAPS (532 nm). Under standard operation, the CAPS performs periodic baselines (i.e. measurements with a particle filter) to correct for the gas phase interference, which derives mainly from nitrogen dioxide (NO_2). This correction is critical in the study of aircraft emissions, as NO_2 levels vary between 0 and 30 ppm during typical jet

engine operation and can fluctuate significantly in short timescales. Using the baseline function under such variable conditions can lead to inaccurate results. Therefore, we used the online NO₂ measurements in the Annex 16 line to correct for the gas phase interference. In order to calibrate the CAPS response to NO₂, laboratory measurements were performed using a NO₂ pressurized gas bottle (composition: NO₂ 20 ppm, O₂ 20 %, N₂ rest) diluted with HEPA filtered air. The results, presented in Fig. S3, reveal a very linear response (out to 6000 Mm⁻¹) for the CAPS extinction signal. The slope retrieved for the extinction measurement (3.2 ppb/Mm⁻¹) corresponds to an absorption cross section for NO₂ at 532 nm of $\sim 1.3 \cdot 10^{-19}$ cm², which agrees fairly well with previously reported values (Osthoff et al., 2006). Moreover, during the measurements of jet engine emissions, a bypass line with an HEPA filter was used to check the gaseous interferences in the CAPS at different thrust and NO₂ levels. In terms of light extinction, these results are in excellent agreement with the laboratory calibration curve. Regarding the scattering signal, this should in principle not be affected by the presence of NO₂. However, as shown in Fig. S3, the scattering signal increased with NO₂ following a third order polynomial. Besides, the curves obtained from the laboratory calibrations and jet engine measurements did not agree in this case. A light leak in the instrument was considered a possible source of these inconsistencies. However, very similar NO₂ interference curves were obtained after the light sealing of the instrument was exchanged. Despite all our efforts, we could not find the origin of the interference in the CAPS scattering signal. The online NO₂ measurements in the raw exhaust line and the laboratory calibration curve were used to correct the CAPS extinction measurements. Although we also tried to use the NO₂ calibration results to correct the CAPS scattering measurements, the results were inconsistent with other instruments.

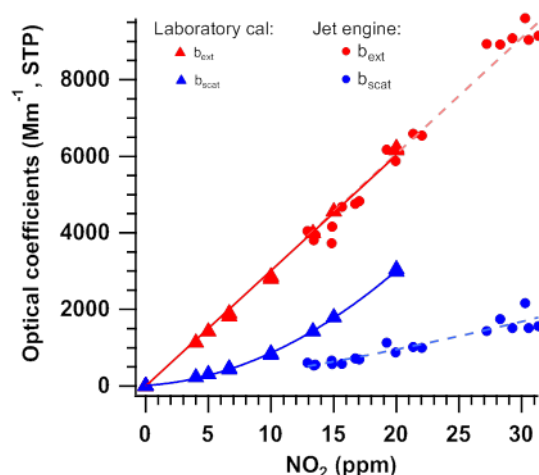


Figure S3. Nitrogen dioxide (NO₂) interference in the Cavity Attenuated Phase Shift PM single scattering albedo monitor (CAPS) extinction and scattering coefficients (b_{ext} and b_{scat}) derived from laboratory calibrations (with NO₂ gas cylinder) and jet engine measurements (with HEPA filter in front of the instrument).

S1.4 Comparison with Mie Theory

To validate the results from the optical instruments, we compared the measurements of AS and Nig at several concentrations with the optical coefficients modeled using Mie theory. For the modelling with Mie theory we used the log-normal fits of the SMPS size distributions and the ranges of literature refractive indexes (RI) reported in Table S2. The AS RI at 532 nm is in the range of 1.50-1.53 (see references in table), with imaginary part equal to zero (purely scattering). The RI of AS is known to be fairly constant over the range of measurement wavelengths deployed in this work, and therefore the same range of RIs was used to validate the measurements at 870 nm. Several works have measured the RI for Nig at 532 nm, which varies between $1.626 + i0.243$ (Flores et al., 2012) and $1.728 + i0.278$ (Bluvstein et al., 2012), but none reported the RI at 870 nm. The spectroscopic ellipsometry measurements reported in Liu et al. (2013) and Bluvstein et al. (2017) show a strong wavelength dependency of the Nig RI, with $1.6 < n < 1.8$ and $0.11 < k < 0.28$ for wavelengths between 200 and 800 nm.

Refractive index (RI= $n+ik$)	n	k	λ (nm)	Reference
Ammonium sulfate (AS)	1.53	1×10^{-7}	532	Toon et al. (1976)
	1.53	0	532	Pettersson et al. (2004)
	1.52	0	532	Abo Riziq et al. (2007)
	1.521 ± 0.0026	0.002 ± 0.002	532	Dinnar et al. (2008)
	1.52 ± 0.01	0.00 ± 0.03	532	Lang-Yona et al. (2009)
	1.521 ± 0.004	0.000 ± 0.008	532	Bluvshstein et al. (2012)
	1.504 ± 0.015	0.000 ± 0.028	532	Flores et al. (2012)
Nigrosin ink (Nig)	1.67	0.26	532	Garvey and Pinnick (1983)
	1.70 ± 0.04	0.31 ± 0.05	532	Lack et al. (2006)
	1.649 ± 0.007	0.238 ± 0.008	532	Dinar et al. (2008)
	1.65 ± 0.01	0.24 ± 0.01	532	Lang-Yona et al. (2009)
	1.72 ± 0.01	0.28 ± 0.08	532	Lang-Yona et al. (2009)
	1.728 ± 0.009	0.278 ± 0.017	532	Bluvshstein et al. (2012)
	1.626 ± 0.021	0.243 ± 0.023	532	Flores et al. (2012)
	1.79*	0.22*	700	Liu et al. (2013)
	1.83*	0.14*	800	Bluvshstein et al. (2017)

Table S2. Literature refractive indexes (RI) of dry ammonium sulfate (AS) and nigrosin (Nig). *The reported RI for nigrosin at 700 and 800 nm were estimated from spectroscopic ellipsometry measurements.

Figure S4 shows the results of the comparison between modeled and measured scattering coefficient at several AS concentrations, using a range of RIs that slightly extends the lower limit of the RIs found in the literature. The color codes in panel (a) and (b) represent the slopes from the linear regression between the predictions from Mie theory varying RI ($1.46 \leq n \leq 1.53$ and $k=0$) and the measurements at (a) 532 nm and (b) 870 nm. At both wavelengths, the best results were found for $RI=1.49+i0.00$, for which both scattering measurements agree with Mie theory within 3 % (panels (c) and (d)). Our best estimate of the AS RI is slightly lower than the literature references in Table S2. This underestimation can be related to the use of the full size distributions instead of size- and mobility- selected particles, as recently shown in the work of Radney and Zangmeister (2018). However, the differences are very small, and good agreement (within 6 %) is still found using $RI = 1.50 + i0.00$. Therefore, we conclude that both instruments can accurately measure the optical coefficients of highly scattering particles.

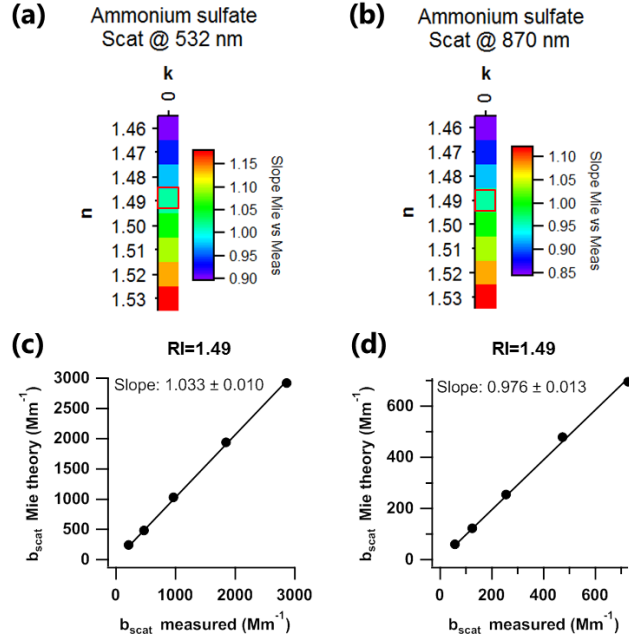


Figure S4. Comparison of the ammonium sulfate (AS) measurements with Mie theory: (a) Slope between modeled and measured scattering coefficient (b_{scat}) at 532 nm varying the real part of the refractive index ($RI=n+ik$); (b) Slope between modeled and measured b_{scat} at 870 nm varying the real part of the RI; (c) Comparison of modeled and measured b_{scat} at 532 nm using our best estimate of the RI; (d) Comparison of modeled and measured b_{scat} at 870 nm using our best estimate of the RI.

The comparison with Mie theory for the measurements with Nig at 870 nm and 532 nm are shown in Figs. S5 and S6, respectively. In contrast to AS, in this case both the real and imaginary part of the RI had to be varied separately and the three optical coefficients (scattering, absorption and extinction) had to be considered for the comparison.

For the measurements at 870 nm, the best agreement with Mie theory predictions was obtained using $RI=1.68 + i0.10$ (Fig. S5 panels (a), (b), and (c)), for which the differences between the three modeled and measured optical coefficients was around 1 % (panels (d), (e), and (f)). Although we could not find literature values of the RI of Nig at this high wavelength, our best estimate for the Nig RI at 870 nm seems to be reasonable if compared to the trend at high wavelengths of the spectroscopic ellipsometry measurements reported in Table S2. Thus, our results seem to indicate that the PAX can accurately measure the optical coefficients of strongly absorbing particles.

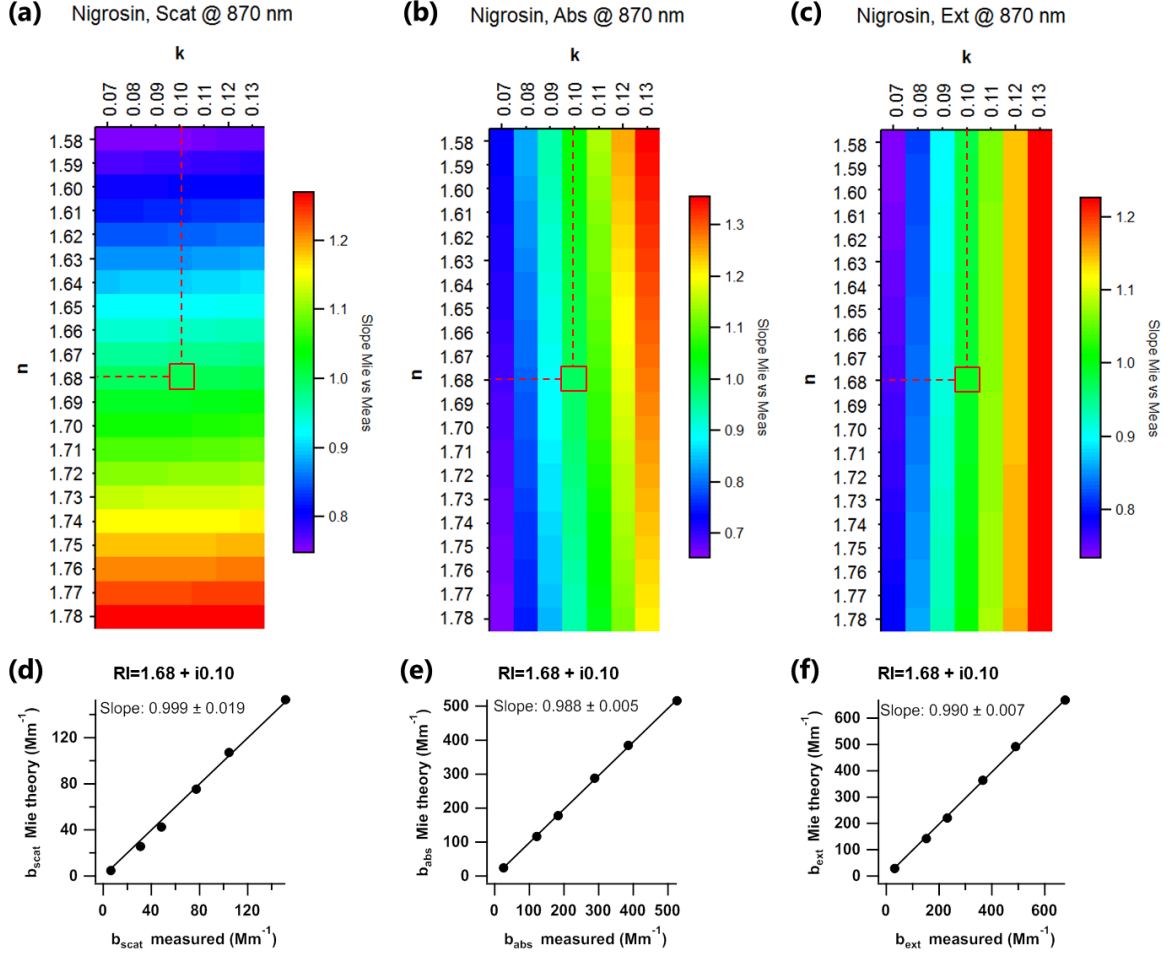


Figure S5. Comparison of the nigrosine (Nig) measurements at 870 nm with Mie theory: (a) Slope between modeled and measured scattering coefficient (b_{scat}) varying the refractive index ($\text{RI}=n+ik$); (b) Slope between modeled and measured absorption coefficient (b_{abs}) varying the RI; (c) Slope between modeled and measured extinction coefficient (b_{ext}) varying the RI; (d) Comparison of modeled and measured b_{scat} using our best estimate of the RI; (e) Comparison of modeled and measured b_{abs} using our best estimate of the RI; (f) Comparison of modeled and measured b_{ext} using our best estimate of the RI

At 532 nm, the comparison with Mie theory did not give such good results (Fig. S6). Although we extended the range of tested RIs to include all combinations of $1.60 \leq n \leq 1.75$ and $0.20 \leq k \leq 0.35$, Mie theory could not reconstruct the absolute values of measured scattering (underestimated by model) and absorption (overestimated by model). In contrast, the extinction measurement could be reproduced within 1 % using an $\text{RI} = 1.60 + i0.22$. As for the AS experiments, this RI value is slightly below the literature range (both n and k), which can again be related to the use of the full size distributions in this work. To obtain a similar agreement for the scattering and absorption coefficients, a $\text{RI} = 1.83 + i0.17$ has to be used, which largely differs from the literature values (unreasonably high n and low k). Thus, we conclude that for strongly absorbing particles the CAPS used in this work seems to properly measure the extinction, but overestimates the scattering (and consequently underestimates absorption).

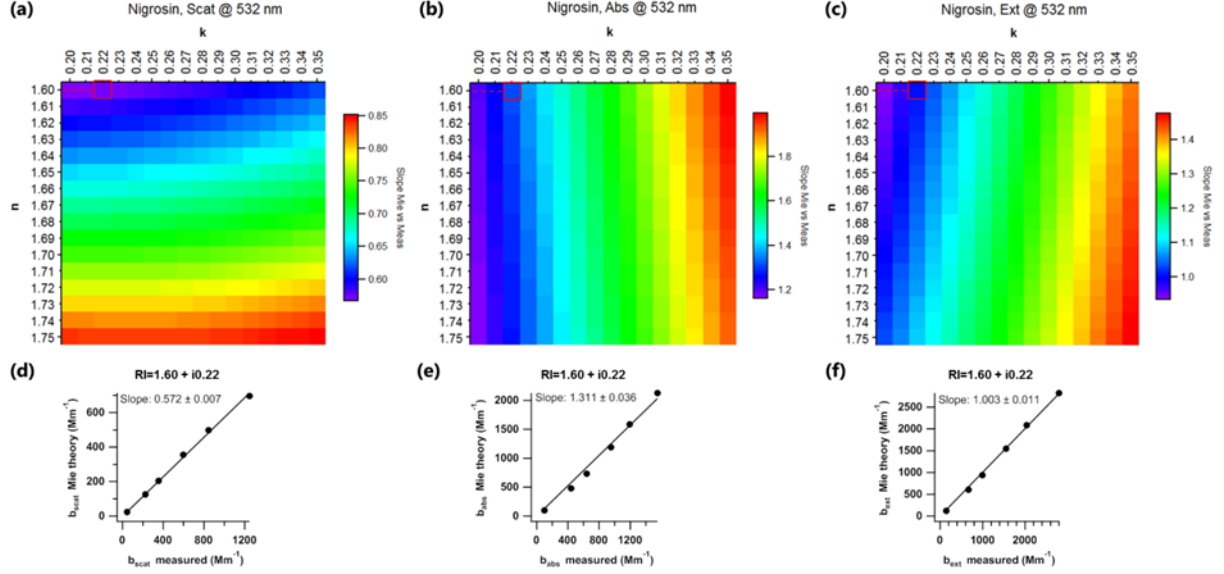


Figure S6. Comparison of the nigrosin (Nig) measurements at 532 nm with Mie theory: (a) Slope between modeled and measured scattering coefficient (b_{scat}) varying the refractive index ($\text{RI}=n+ik$); (b) Slope between modeled and measured absorption coefficient (b_{abs}) varying the RI; (c) Slope between modeled and measured extinction coefficient (b_{ext}) varying the RI; (d) Comparison of modeled and measured b_{scat} using our best estimate of the RI; (e) Comparison of modeled and measured b_{abs} using our best estimate of the RI; (f) Comparison of modeled and measured b_{ext} using our best estimate of the RI

As shown in the previous section, inconsistencies in the CAPS scattering signal were also observed in the NO₂ interference calibration. Despite all our efforts, we could not find the problem in the CAPS scattering measurement or a way to properly correct it. Therefore, we derived the CAPS scattering coefficient using the PAX absorption measurement and a thrust dependent absorption Ångström exponent (AAE) obtained from aircraft engine measurements with a seven-wavelength aethalometer, as explained below.

S1.5 Calculation of scattering at 532 nm

The data from a 7-wavelength aethalometer (model AE-33, Magee scientific) collected in a previous measurement campaign with the same type of engine (CFM56-7B/26) and Jet A-1 fuel, was used to estimate the AAE of the PM emissions at the engine exit plane. The AAE was calculated using the aethalometer data at 520 nm and 880 nm, selected for being close to the CAPS and PAX operating wavelengths, as follows:

$$\text{AAE} = -\frac{\ln\left(\frac{b_{\text{abs},520}}{b_{\text{abs},880}}\right)}{\ln\left(\frac{520}{880}\right)} \quad (\text{S1})$$

The power fit to the thrust dependent AAE reported in Fig. S7 was then used together with Eq. (S1) to derive the absorption coefficient at the CAPS measurement wavelength ($b_{\text{abs},532}$) from the PAX absorption coefficient ($b_{\text{abs},870}$). Lastly, the CAPS scattering was determined as the difference between the measured extinction and the calculated absorption at 532 nm.

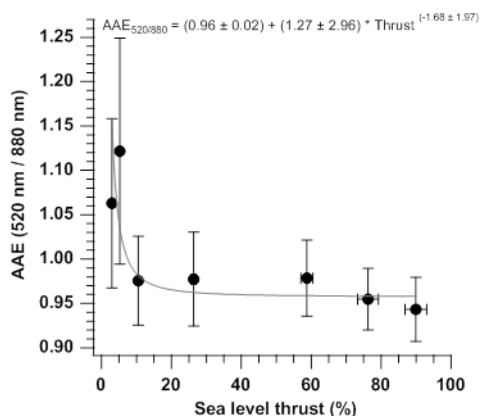


Figure S7. Thrust dependent absorption Ångstrom exponent (AAE) determined from aethalometer measurements at 520 and 880 nm.

S2 Results and discussion

S2.1 EC/OC analysis

Table S3 presents an overview of the results from the EC/OC analysis. While the concentration of EC in the back-up filters ($EC_{\text{back-up}}$) was negligible within the uncertainties, the positive artifact of gaseous OC adsorbing onto the filters surface ($OC_{\text{back-up}}$) represented around 43 % of OC_{main} (see Fig. S8). The corrected OC concentrations (OC_{corr}) were calculated by subtracting $OC_{\text{back-up}}$ from OC_{main} , and OC_{corr} was then used to calculate the total carbon ($TC = EC_{\text{main}} + OC_{\text{corr}}$) and the OC fraction (OC/TC). Table S4 contains the parameters required to calculate emission indexes (EI) from the mass concentrations (i.e. CO_2 , CO and total hydrocarbons concentrations), the calculated EI for EC ($EI_{m,EC}$) and the particles' size parameters (geometric mean diameter (GMD) and geometric standard deviation (GSD)). Figure S9 shows the thermograms of the EC/OC analysis of the samples taken at low-, medium-, and high-thrust levels during measurements with Jet A-1 fuel.

	Thrust (%)	OC _{back-up} ($\mu\text{g m}^{-3}$)	OC _{main} ($\mu\text{g m}^{-3}$)	OC _{corr} ($\mu\text{g m}^{-3}$)	EC _{back-up} ($\mu\text{g m}^{-3}$)	EC _{main} ($\mu\text{g m}^{-3}$)	TC ($\mu\text{g m}^{-3}$)	OC/TC
Jet A-1	95.6	0.68 ± 0.13	1.64 ± 0.18	0.96 ± 0.22	-0.02 ± 0.10	4.63 ± 0.33	5.60 ± 0.39	0.17 ± 0.24
	77.4	0.49 ± 0.07	1.22 ± 0.11	0.72 ± 0.13	0.03 ± 0.05	3.01 ± 0.20	3.74 ± 0.24	0.19 ± 0.19
	64.0	0.24 ± 0.04	0.80 ± 0.07	0.56 ± 0.08	0.02 ± 0.03	2.10 ± 0.14	2.65 ± 0.16	0.21 ± 0.16
	52.7	0.11 ± 0.02	0.36 ± 0.03	0.24 ± 0.03	0.00 ± 0.01	0.74 ± 0.05	0.99 ± 0.06	0.25 ± 0.15
	28.8	0.08 ± 0.01	0.28 ± 0.02	0.20 ± 0.02	0.00 ± 0.01	0.06 ± 0.01	0.26 ± 0.03	0.78 ± 0.16
	5.2*	0.04 ± 0.01	0.14 ± 0.01	0.10 ± 0.01	0.00 ± 0.01	0.01 ± 0.01	0.11 ± 0.01	0.90 ± 0.16
	2.7	0.15 ± 0.02	0.39 ± 0.03	0.24 ± 0.03	0.00 ± 0.01	0.08 ± 0.01	0.32 ± 0.04	0.75 ± 0.17
HEFA 32 %	96.2	0.57 ± 0.08	1.19 ± 0.12	0.61 ± 0.14	0.01 ± 0.06	3.93 ± 0.26	4.55 ± 0.29	0.14 ± 0.24
	96.0	0.44 ± 0.08	1.14 ± 0.11	0.70 ± 0.14	0.01 ± 0.06	3.89 ± 0.25	4.59 ± 0.29	0.15 ± 0.21
	94.2	0.78 ± 0.12	1.54 ± 0.16	0.76 ± 0.20	0.00 ± 0.09	4.12 ± 0.29	4.88 ± 0.36	0.16 ± 0.28
	85.1	0.35 ± 0.06	0.91 ± 0.09	0.57 ± 0.11	0.00 ± 0.05	3.12 ± 0.20	3.69 ± 0.23	0.15 ± 0.20
	83.2	0.44 ± 0.07	1.00 ± 0.09	0.55 ± 0.12	0.00 ± 0.05	3.16 ± 0.21	3.71 ± 0.24	0.15 ± 0.22
	63.3	0.20 ± 0.03	0.51 ± 0.05	0.32 ± 0.06	0.00 ± 0.02	1.59 ± 0.10	1.91 ± 0.12	0.17 ± 0.19
	62.5	0.36 ± 0.04	0.68 ± 0.05	0.31 ± 0.07	0.02 ± 0.02	1.43 ± 0.09	1.74 ± 0.11	0.18 ± 0.22
	29.3	0.08 ± 0.01	0.23 ± 0.02	0.15 ± 0.02	0.00 ± 0.01	0.03 ± 0.01	0.18 ± 0.02	0.84 ± 0.17
	2.8	0.23 ± 0.03	0.60 ± 0.04	0.36 ± 0.05	0.00 ± 0.01	0.04 ± 0.02	0.40 ± 0.05	0.90 ± 0.19

*Integrated sample that includes 65 min of Jet A-1, 70 min of HEFA 5 % and 70 min of HEFA 10 %

Table S3. Overview of the results of the analysis of organic carbon (OC) and elemental carbon (EC).

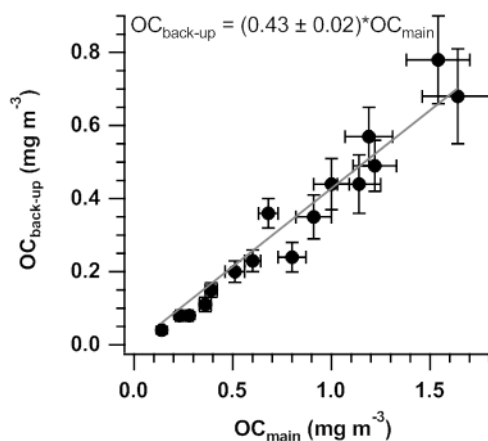


Figure S8. Scatter plot of organic carbon (OC) mass concentration in the back-up filter (positive artifact) and the main filter (positive artifact + real OC).

	Thrust (%)	CO ₂ * (ppm)	CO ** (ppm)	THC (ppm)	El _{m,EC} (mg kg _{fuel} ⁻¹)	GMD (nm)	GSD (nm)
Jet A-1	95.6	45101.5	30.4	16.4	166.4 ± 11.8	42.4 ± 0.6	1.91 ± 0.05
	77.4	40793.8	17.2	9.1	119.8 ± 8.0	36.5 ± 0.3	2.02 ± 0.04
	64.0	36546.1	14.5	12.7	93.2 ± 6.0	32.1 ± 0.2	2.10 ± 0.03
	52.7	33274.3	12.9	7.7	36.4 ± 2.4	27.0 ± 0.1	2.12 ± 0.02
	28.8	28471.7	31.2	11.0	3.3 ± 0.6	17.2 ± 0.1	1.89 ± 0.01
	5.2*	20726.1	303.6	71.6	0.9 ± 0.3	9.0 ± 0.1	1.93 ± 0.02
	2.7	23230.7	753.4	295.1	5.5 ± 0.9	7.9 ± 0.1	1.94 ± 0.02
HEFA 32 %	96.2	44803.0	25.0	9.7	141.5 ± 9.2	40.1 ± 0.4	1.98 ± 0.04
	96.0	44170.7	22.2	10.2	141.9 ± 9.3	38.4 ± 0.4	2.02 ± 0.04
	94.2	44459.0	27.1	10.2	149.3 ± 10.7	39.1 ± 0.5	1.99 ± 0.05
	85.1	41531.6	19.0	9.0	122.6 ± 8.0	35.9 ± 0.3	2.04 ± 0.04
	83.2	41559.1	17.7	9.0	120.9 ± 7.9	36.6 ± 0.2	2.06 ± 0.03
	63.3	36323.7	13.4	8.0	70.9 ± 4.5	30.1 ± 0.2	2.13 ± 0.03
	62.5	36160.0	13.8	7.8	63.8 ± 4.1	29.5 ± 0.2	2.17 ± 0.03
	29.3	28237.1	28.3	7.8	1.7 ± 0.4	15.2 ± 0.1	1.84 ± 0.01
	2.8	22969.8	769.7	306.2	2.6 ± 1.1	6.6 ± 0.1	2.06 ± 0.02

*CO₂ measured in the PM line corrected for dilution; ** CO corrected for wet measurement conditions

Table S4. Thrust and fuel dependent carbon dioxide (CO₂), carbon monoxide (CO) and total hydrocarbons (THC) concentrations for the calculation of emission indexes, calculated emission index of elemental carbon (El_{m,EC}), and particles size parameters (geometric mean diameter (GMD) and geometric standard deviation (GSD)) obtained from the fit of the size distributions.

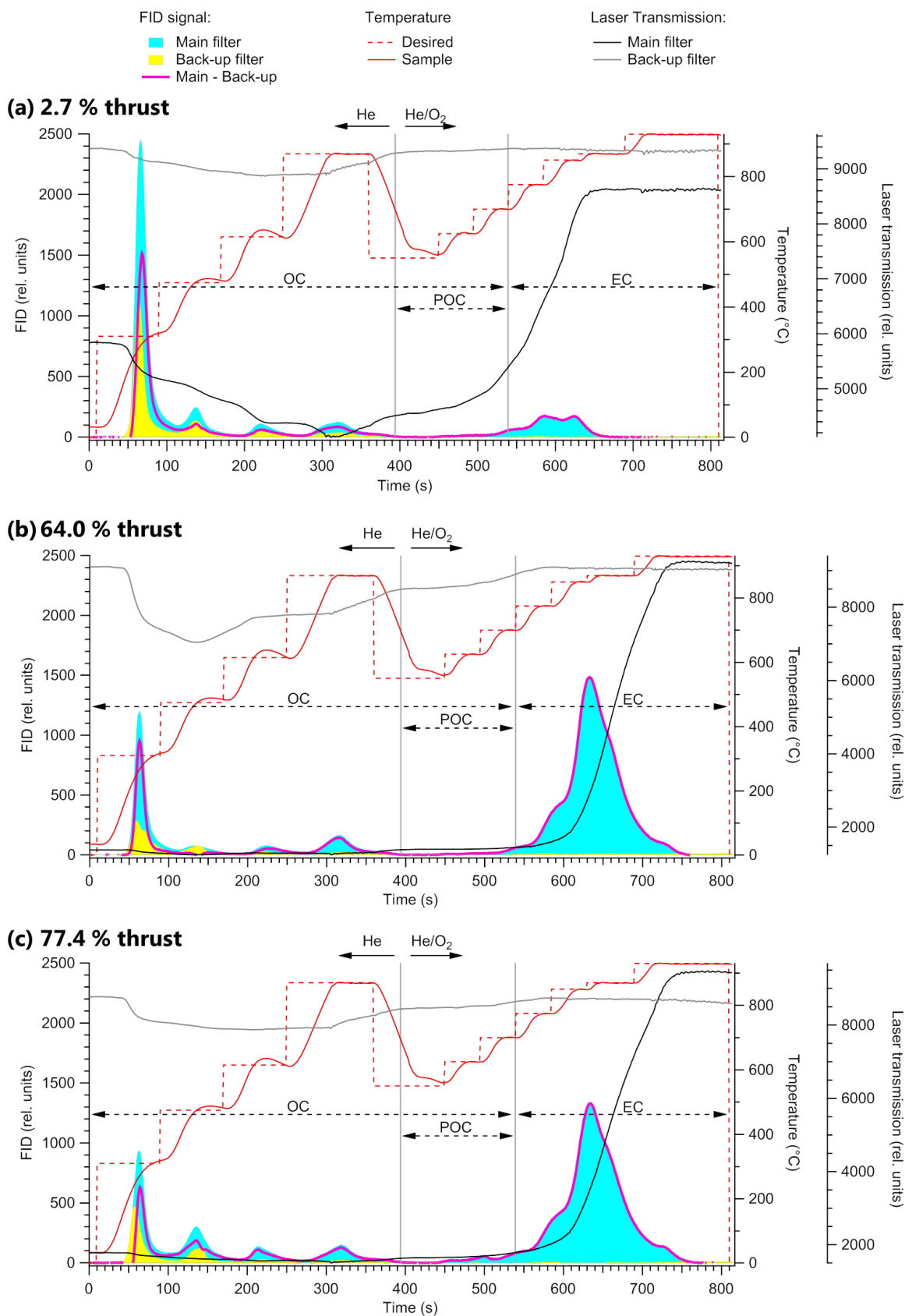


Figure S9. Thermograms used for the quantification of elemental carbon (EC) and organic carbon (OC) emitted from an aircraft engine operated with Jet A-1 fuel at: (a) 3 % thrust, (b) 64 % thrust, and (c) 77 % thrust.

S2.2 Geometric mean particle diameter and geometric standard deviation

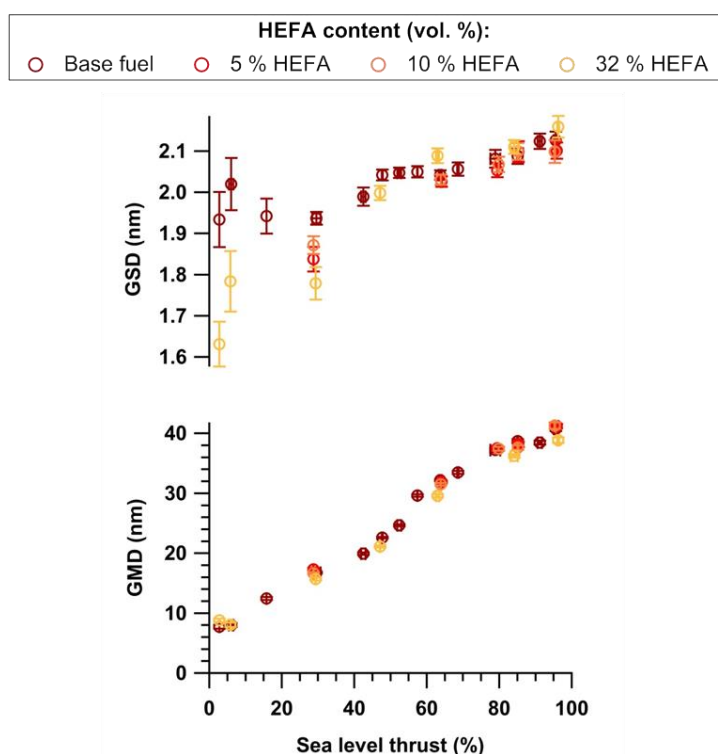


Figure S10. Geometric mean diameter (GMD, bottom) and geometric standard deviation (GSD, top) of the particulate matter (PM) size distributions at the engine exit plane for different thrust levels and HEFA blends.

S2.3 Optical properties

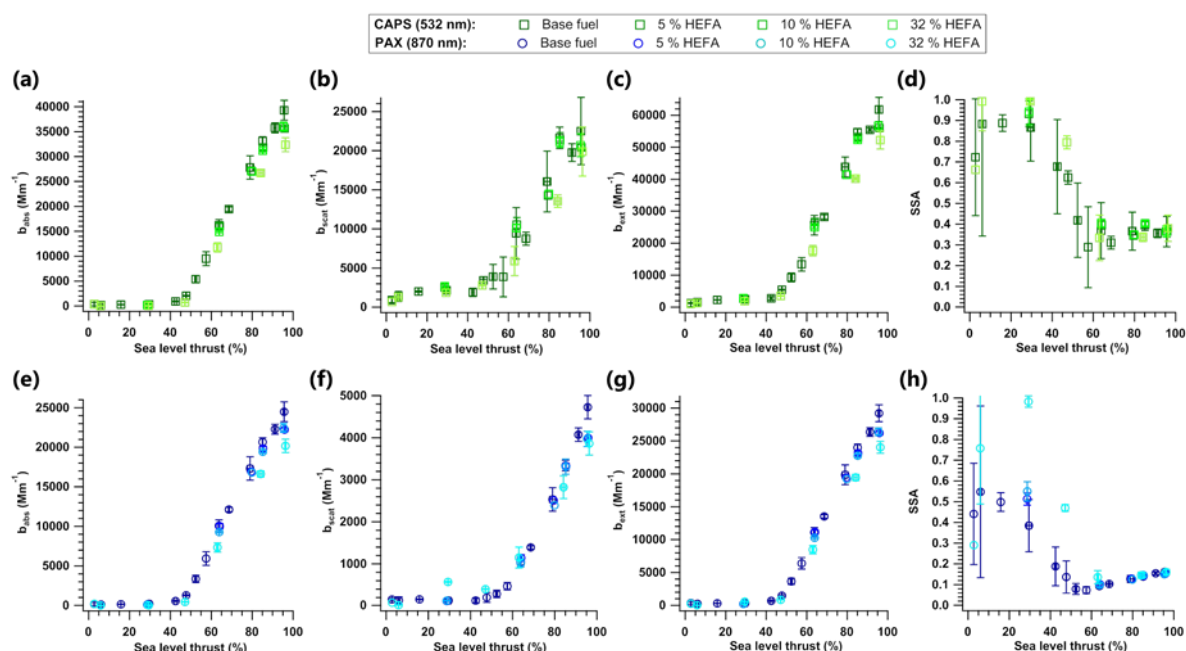


Figure S11. Thrust dependency of the (a) absorption coefficient (b_{abs}), (b) scattering coefficient (b_{scat}), (c) extinction coefficient (b_{ext}) and (d) single scattering albedo (SSA) measured at 532 nm (CAPS) using Jet A-1 fuel and three HEFA blends. (e), (f), (g) and (h): same than above but for measurements at 870 nm (PAX).

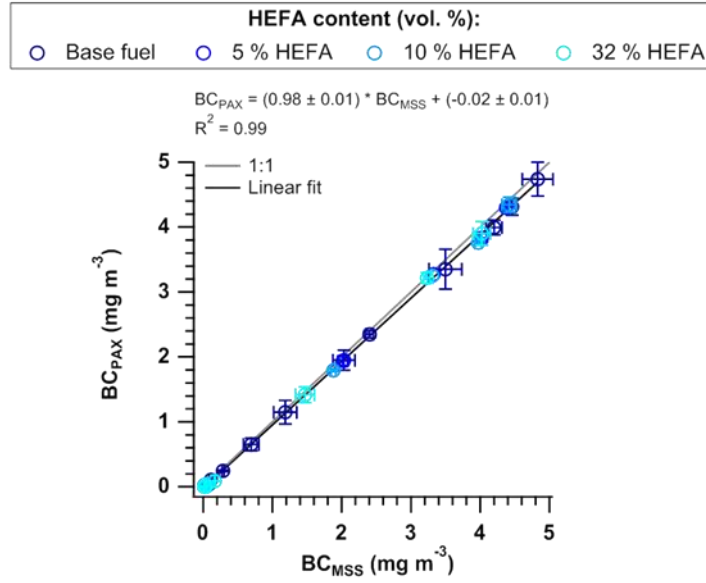


Figure S12. Scatter plot of black carbon mass concentration measured with the photoacoustic extinctions (BC_{PAX}) and the micro soot sensor (BC_{MSS}) for different fuel blends.

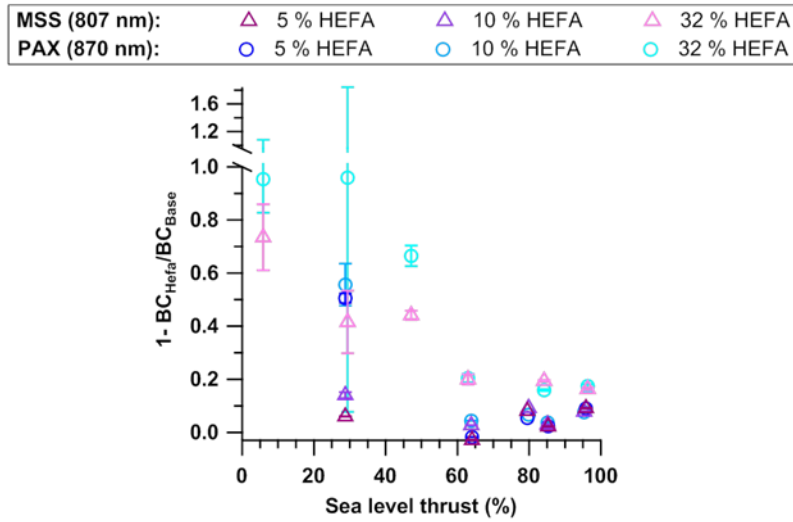


Figure S13. Thrust dependent decrease in the black carbon mass concentration measured with the micro soot sensor (BC_{MSS}) and the photoacoustic extinctions (BC_{PAX}) for the three HEFA blends in comparison to the base Jet A-1 fuel. As for elemental carbon (EC) mass concentration, the decrease due to the 32 % HEFA blend was highest at low thrust levels (e.g. at 6 % thrust BC_{MSS} decreases by 74 % and BC_{PAX} by 95 %), while thrust levels above 60 % were characterized by a lower and rather constant decrease (around 20 % decrease in both BC measurements). The two instruments reported the same BC reduction at high thrust (i.e. high BC mass concentration), but disagreed increasingly as the BC mass concentration decreased for decreasing thrust. This was attributed to the low sensitivity and high noise of the PAX at concentrations $<10 \mu\text{g m}^{-3}$ relative to the MSS.

S2.4 Radiative forcing

Figure S14 reports the wavelength dependent parameters used for the calculation of the simple forcing efficiency (SFE) as defined in Eq. (4) in the manuscript. The solar radiation spectrum (S_0 , in W m^{-2} per nm of bandwidth) was set to the synthetic reference spectrum of solar irradiance at the top of the atmosphere developed by Gueymard (2004). The atmospheric transmission (T_{atm}) was evaluated for cruise conditions ($z = 12 \text{ km}$) using the Simple Model of the Atmospheric Radiative Transfer of Sunshine (SMARTS) model (version 2.9.5, Gueymard, 2001). The atmospheric conditions in the SMARTS model were defined using the 1976 U.S. Standard Atmosphere

(United States Committee on Extension to the Standard Atmosphere, 1976); water vapor and ozone were calculated from the standard atmosphere at $z=12$ km; the reference gaseous absorption model was modified for the case of light pollution; the aerosol optical depth at 550 nm (τ_{550}) was calculated with the empirical relationship $\tau_{550}=\exp(-3.2755-0.15078z)$ (valid for $z > 6$ km) following the recommendations in the SMARTS manual; and the absolute air mass was set to 1.5 (AIM1.5), corresponding to a solar zenith angle of 48.2° (temperate latitudes). The wavelength dependent mass absorption and scattering cross sections (MAC and MSC, respectively) were determined by fitting the measurements (at 532 and 870 nm) with Eqs. (5) and (6) in the manuscript (Fig. S14b).

Although previous works have proposed the use of a cloud fraction (F_c) of 0.6, Hassan et al. (2015) showed that Eq. (4) only performs properly when F_c is set to zero, while it gives unrealistic results when clouds are present. This is because the equation assumes that aerosols below or above clouds can be neglected, which is obviously incorrect and not supported by observations. Therefore, we only considered the case of $F_c = 0$.

The surface spectral albedos “Water or calm ocean”, “Perennial rye grass”, “Light soil”, and “Fresh dry snow” incorporated in the SMARTS model from the Jet Propulsion Laboratory Advanced Spaceborne Thermal Emission and Reflection Radiometer (ASTER) spectral reflectance database (Hook, 2018) were used to represent ground surfaces covered by sea water, grass, soil and snow, respectively. In absence of backscattering measurements, the backscattering fraction (β) was estimated with Mie theory, using the measured size parameters at cruise conditions for pure Jet A-1 fuel (GMD = 29.6 nm and GSD = 2.0 nm at 57.4 % thrust) and the range of refractive indexes suggested by Bond and Bergstrom (2007) (i.e. $m=1.75+i0.63$ to $m=1.95+i0.79$), which lead to $\beta = 0.27 \pm 0.01$.

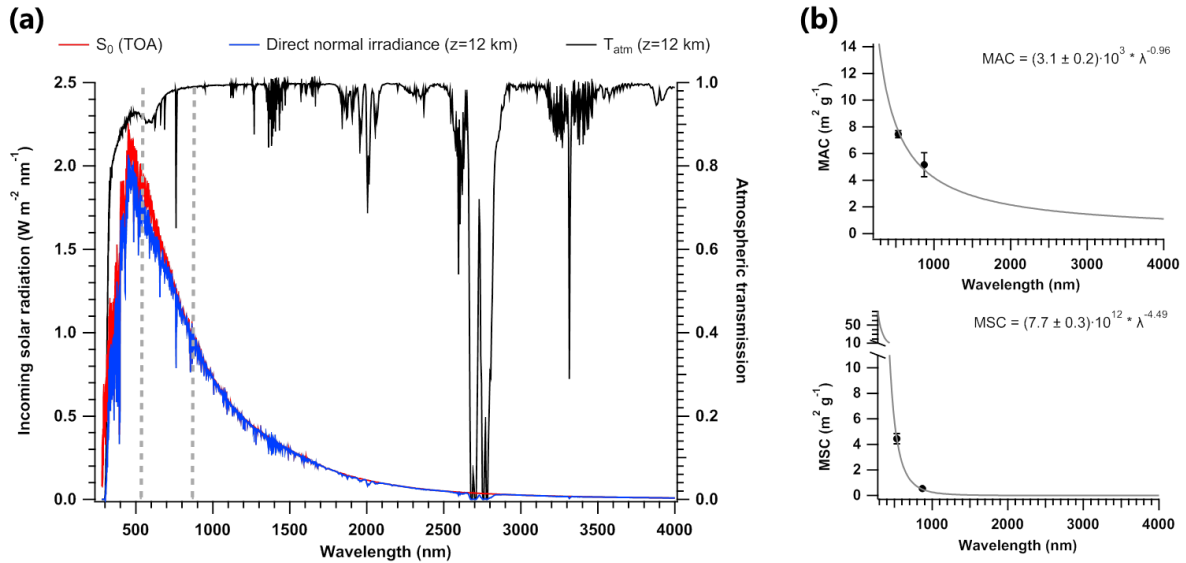


Figure S14. (a) Incoming solar radiation spectrum (S_0 , Gueymard et al., 2004) and calculated direct normal radiation and atmospheric transmission (T_{atm}) at cruise height ($z = 12$ km); (b) Inverse wavelength fit to the mass absorption cross section (MAC; top) and mass scattering cross section (MSC; bottom) measured at 532 and 870 nm.

The SFE spectral dependence of the fresh PM emissions during cruise conditions is shown in Fig. S15 for the four different ground types (i.e. surface albedos) considered in this work. Positive SFE indicates a warming effect; negative SFE corresponds to cooling. The high surface albedo of snow ($a_{snow} = 0.5-1.0$ for $\lambda < 1400$ nm), translated into a strong positive SFE, especially in the visible range. The highest spectral forcing over snow $SFE_{snow} = 16.5 W g^{-1} nm^{-1}$ was found at the blue wavelength (450 nm). The lower surface albedos from grass and soil (on average $a_s = 0.2$ for both surface types) induced a moderate SFE, which even turned negative (i.e. cooling) at short wavelengths ($\lambda < 425$ nm for soil and $\lambda < 500$ nm for grass). However, the overall dominant effect was warming, with a maximum SFE of $2.5 W g^{-1} nm^{-1}$ found in the red visible range (between 700-760 nm) for both surface types. In contrast, the extremely low surface albedo from sea surfaces ($a_{sea} = 0.004-0.04$) yielded very small SFE, which

was mainly negative and had a minimum of $-2.8 \text{ W g}^{-1} \text{ nm}^{-1}$ at 330 nm. Figure S15 also contains the integrated forcing (in W g^{-1}) in the spectral range 450-2000 nm (limited by the availability of albedo data) for the four surface types. The strongest warming effect of the fresh aircraft PM was observed when the emissions occurred above highly reflective surfaces like snow. The integrated SFE in this case was in the order of 4700 W g^{-1} . Other land surfaces (i.e. soil and grass) showed a moderate warming, with an integrated SFE in the range of 800 to 1500 W g^{-1} . The integrated effect of the emissions over dark surfaces like sea water was extremely low ($\sim 90 \text{ W g}^{-1}$) and, contrary to the other surface types, the overall effect was cooling.

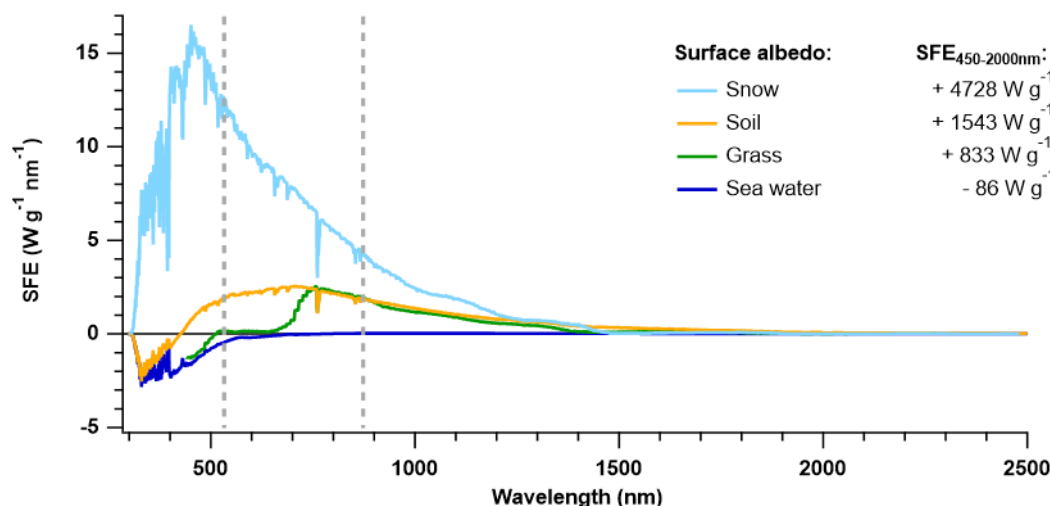


Figure S15. Simple forcing efficiency (SFE) spectra for aircraft engine PM over different surface types, including sea water, grass, soil and snow, and integrated spectral values for the four surface types.

This simple model does not consider the effects from underlying clouds. However, aircraft cruising altitude (10 – 13 km above sea level) normally exceeds the typical cloud top altitude (except in tropical latitudes). Samset and Myhre (2015) studied the differences in the modeled altitude dependence of the direct radiative forcing (DRF) of BC when clouds are taken into consideration, and found that globally the DRF of BC at cruise altitude (100 hPa) was doubled when using all-sky conditions ($\sim 2300 \text{ W g}^{-1}$) compared to clear-sky conditions ($\sim 1000 \text{ W g}^{-1}$). In a first approximation, we expect that cruise emissions above clouds will induce similar radiative effects to the emissions over snow-covered surfaces (i.e. strong warming). In addition, our estimates of the radiative forcing correspond only to fresh aircraft PM emissions and do not take into account the atmospheric aging of the particles in the emission plume. Plume evolution studies including the measurement of the particles' optical properties and complex models are required for an accurate estimate of the radiative effects of aircraft PM emissions.

References

- Abo Riziq, A., Erlick, C., Dinar, E., and Rudich, Y.: Optical properties of absorbing and non-absorbing aerosols retrieved by cavity ring down (CRD) spectroscopy, *Atmos. Chem. Phys.*, 7, 1523-1536, doi:10.5194/acp-7-1523-2007, 2007.
- Bluvshstein, N., Flores, J. M., He, Q., Segre, E., Segev, L., Hong, N., Donohue, A., Hilfiker, J. N., and Rudich, Y.: Calibration of a multi-pass photoacoustic spectrometer cell using light-absorbing aerosols, *Atmos. Meas. Tech.*, 10, 1203–1213, doi:10.5194/amt-10-1203-2017, 2017.
- Bluvshstein, N., Flores, J. M., Abo Riziq, A., and Rudich, Y.: An approach for faster retrieval of aerosols' complex refractive index using cavity ring-down spectroscopy, *Aerosol Sci. Technol.*, 46, 1140-1150, doi:10.1080/02786826.2012.700141, 2012.

Bond, T. C., and Bergstrom R. W.: Light absorption by carbonaceous particles: An investigative review, *Aerosol Sci. Tech.*, 40, 27-67, doi:10.1080/02786820500421521, 2007.

Dinar, E., Abo Riziq, A., Spindler, C., Erlick, C., Kiss, G., and Rudich, Y.: The complex refractive index of atmospheric and model humic-like substances (HULIS) Retrieved by a cavity ring down aerosol spectrometer (CRD-AS). *Faraday Discuss.*, 137, 279–295, doi:10.1039/B703111D, 2008.

Flores, J. M., Bar-Or, R. Z., Bluvshstein, N., Abo Riziq, A., Kostinski, A., Borrmann, S., Koren, I., and Rudich, Y.: Absorbing aerosols at high relative humidity: linking hygroscopic growth to optical properties, *Atmos. Chem. Phys.*, 12, 5511–5521, doi:10.5194/acp-12-5511-2012, 2012.

Garvey, D.M., and Pinnick, R.G.: Response characteristics of the particle measuring systems active scattering aerosol spectrometer probe (Asasp-X), *Aerosol Sci. Technol.*, 2, 477-488, doi: 10.1080/02786828308958651, 1983.

Gueymard, C.: Parameterized transmittance model for direct beam and circumsolar spectral irradiance, *Solar Energy*, 71, 325-346, doi:10.1016/S0038-092X(01)00054-8, 2001.

Gueymard, C.: The sun's total and spectral irradiance for solar energy applications and solar radiation models, *Solar Energy*, 76, 423-453, doi:10.1016/j.solener.2003.08.039, 2004.

Hassan T., Moosmueller, H., and Chung, C. E.: Coefficients of an analytical aerosol forcing equation determined with a Monte-Carlo radiation model, *J. Quant. Spectrosc. Radiat. Transf.*, 164, 129-136, doi:10.1016/j.jqsrt.2015.05.015, 2015.

Hook, S. J.: ECOSTRESS spectral library, Jet Propulsion Laboratory, California Institute of Technology, <http://speclib.jpl.nasa.gov>, last access: 26 April 2018.

ICAO: Annex 16 to the Convention on International Civil Aviation, Environmental Protection, Volume II Aircraft Engine Emissions, Fourth Edition, 2017.

Jonsdottir, H.R., Delaval, M., Leni, Z., Keller, A., Brem, B.T., Siegerist, F., Schönenberger, D., Durdina, L., Elser, M., Burtscher, H., Liati, A., and Geiser, M.: Non-volatile particle emissions from aircraft turbine engines at ground-idle induce oxidative stress in bronchial cells, *Commun. Biol.*, 2, 90, doi:10.1038/s42003-019-0332-7, 2019.

Lack, D. A., Lovejoy, E. R., Baynard, T., Pettersson, A., and Ravishankara, A. R.: Aerosol absorption measurement using photoacoustic spectroscopy: sensitivity, calibration, and uncertainty developments, *Aerosol Sci. Technol.*, 40, 697-708, doi:10.1080/02786820600803917, 2006.

Lang-Yona, N., Rudich, Y., Segre, E., Dinar, E., and Abo Riziq, A.: Complex refractive indices of aerosols retrieved by continuous wave-cavity ring down aerosol spectrometer, *Anal. Chem.*, 81, 1762–1769, doi:10.1021/ac8017789, 2009.

Liu, P., Zhang, Y., and Martin, S. T.: Complex refractive indices of thin films of secondary organic materials by spectroscopic ellipsometry from 220 to 1200 nm, *Environ. Sci. Technol.*, 47, 13594–13601, doi:10.1021/es403411e, 2013.

Osthoff, H. D., Brown, S. S., Ryerson, T. B., Fortin, T. J., Lerner, B. M., Williams, E. J., Pettersson, A., Baynard, T., Dube, W. P., Ciciora, S. J., and Ravishankara, A. R.: Measurement of atmospheric NO₂ by pulsed cavity ring-down spectroscopy, *J. Geophys. Res.*, 111, D12305, doi:10.1029/2005JD006942, 2006.

Pettersson, A., Lovejoy, E. R., Brock, C. A., Brown, S., and Ravishankara, A. R.: Measurement of aerosol optical extinction at 532 nm with pulsed cavity ring down spectroscopy, *J. Aerosol Sci.*, 35, 995–1011, doi:10.1016/j.jaerosci.2004.02.008, 2004.

Radney, J. G., and Zangmeister, C. D.: Comparing aerosol refractive indices retrieved from full distribution and size- and mass-selected measurements, *J. Quant. Spectrosc. Radiat. Transf.*, 220, 52-66, doi:10.1016/j.jqsrt.2018.08.021, 2018.

Samset, B. H., and Myhre, G.: Climate response to externally mixed black carbon as a function of altitude, *J. Geophys. Res. Atmos.*, 120, 2913-2927, doi:10.1002/2014JD022849, 2015.

Toon, O. B., and Pollack, J. B.: The optical constants of several atmospheric aerosol species: ammonium sulfate, aluminum oxide, and sodium chloride, *J. Geophys. Res. Atmos.*, 81, 5733-5748, doi: 10.1029/JC081i033p05733, 1976.

United States Committee on Extension to the Standard Atmosphere, "U.S. Standard Atmosphere, 1976", National Oceanic and Atmospheric Administration, National Aeronautics and Space Administration, United States Air Force, Washington D.C., 1976.